Electronic Supplementary Information

Dynamic-Self-Catalysis as Accelerated Air-Cathode for Rechargeable Near-Neutral Zn-air Batteries with Ultrahigh Energy Efficiency

Tianran Zhang,*[a, †] Xiao Feng Lim, [b, †] Shengliang Zhang, [c,†] Jian Zheng, [a] Xiangfeng Liu [a] and Jim Yang Lee *[b]

[a] College of Material Science and Opto-Electronic Technology, University of Chinese Academy of Sciences, China

[b] Department of Chemical and Biomolecular Engineering, National University of Singapore, 4 Engineering Drive 4, Singapore, 117576, Singapore

[c] College of Materials Science and Technology, Nanjing University of Aeronautics and Astronautics, Nanjing, China

Experimental Section

Preparation of Electrolytes

An aqueous near-neutral electrolyte was formulated with 2 M NH_4Cl (≥ 99.5 %, Sigma Aldrich), 0.5 M $ZnCl_2$ (anhydrous, Sigma Aldrich), and different concentrations (0.04, 0.1 and 0.2 M) of $MnSO_4$ (monohydrate, ≥ 99 %, Sigma Aldrich) and $CuCl_2$ (0.02, 0.04, 0.1 M) (≥ 97 %, Sigma Aldrich). Some investigations also made use of electrolytes with 0.4 M NH_4Cl, 0.4 M $ZnCl_2$, 0.04 M $MnCl_2$ (tetrahydrate, ≥ 98 %, Sigma Aldrich) and 0.1 M CuCl2, or with 0.4 M (NH4)2SO4 (≥ 99.5 %, Merck), 0.4 M $ZnSO_4$ (heptahydrate, ≥ 99.0%, Sigma Aldrich), 0.04 M $MnSO_4$ and 0.1 M $CuSO_4$ (pentahydrate, ≥ 99.5%, Nacalai Tesque, Inc.). The electrolytes are firstly treated by cyclic voltammetry measurements with a three-electrode system (a carbon paper as the working electrode, a Pt foil as the counter electrode and an Ag/AgCl electrode (3 M KCl, aq) as the reference electrode) for 20 cycles in the potential range of -0.2 V to 0.7 V vs. Ag/AgCl before their usage in Zn-air batteries.

Assembling and Evaluation of Rechargeable Zinc-air Battery (ZAB)

Rechargeable Zn-air batteries with the dynamic self-catalysis design (DSC-ZAB) was assembled with a Zn foil anode, a commercial carbon paper (HESEM, HCP020N) as the air cathode, a gas diffusion layer (GDL) and a specifically formulated electrolyte. An anion exchange membrane (AEM, AMI7001, Huamo Tech) segregated the cell into the (Zn) anode compartment and the (air) cathode compartment. The electrolyte in the anode compartment (anolyte) had the same NH_4Cl and $ZnCl_2$ concentrations as in the air cathode compartment (catholyte). But the Cu(II) and Mn(II) additives were added into the air cathode compartment. The volumes of both the catholyte and anolyte were 3.5 ml. The commercial carbon paper (2cm x 2cm) with thickness of 0.2 mm and weight of 0.78 g cm^{-3} was electrochemically acidified to improve its hydrophilicity (Fig. S1). Specifically, the carbon paper served as the working electrode, together with a graphite rod counter electrode and an Ag/AgCl (3 M KCl, aq) reference electrode. The electrolyte was 0.5 M H_2SO_4 (95~97 %, Merck). A potential of 1.6 V *vs.* Ag/AgCl was applied for 20 minutes. The treated carbon paper was rinsed with deionized water and dried overnight in the air. For comparison, standard rechargeable near-neutral Zn-air batteries were assembled using a Zn anode, a catalyst-loaded carbon paper air cathode and a 2 M NH_4Cl and 0.5 M

$ZnCl_2$ aqueous electrolyte. The 20 wt% Pt/C and IrO_2 mixture were used as the catalyst (mass ratio 1:1) with mass loading of 1 mg cm^{-2}. Galvanostatic charge/discharge (GCD) was performed at a current density of 0.5 mA cm^{-2} for 4 hours per cycle (2 hours discharge then charge). Rate performance at 1 mAh cm^{-2} capacity was evaluated at current densities of 0.5, 1.0, 2.0 and 5.0 mA cm^{-2}. Battery stability was measured at 0.5 mA cm^{-2} for 4 h per cycle and the long-term stability was evaluated with an areal capacity of 10 mA cm^{-2} (1.0 mA cm^{-2} for 20 hours per cycle). Cyclic voltammetry was performed in the 0.75 V – 2.30 V *vs*. Zn potential range at 1 mV s^{-1}. Specific capacity was normalized by the amount of Zn consumed. The energy efficiency of the ZAB was calculated by the following equation:

$$\text{Energy efficiency (\%)} = \frac{\int_0^t V_{discharge} * J_{discharge} * tdt}{\int_0^t V_{charge} * J_{charge} * tdt} * 100\%. \quad (1)$$

where V, J, t are the discharge or charge voltage, current density, and time respectively.

Charaterizations

X-ray photoelectron spectroscopy (XPS) was conducted with a Kratos Axis Ultra DLD spectrometer (Kratos Analytical Ltd) with an Al K_α X-ray source (1486.71 eV). The measured binding energies were corrected by adjusting the C 1s peak of adventitious carbon to 284.5 eV. Field Emission Scanning Electron Microscopy (FESEM) and Energy Dispersive Spectroscopy (EDS) were performed with a JEOL JSM7610Plus. Field emission transmission electron microscopy (FETEM) images were taken by a JEOL 2010F microscope. The in-situ Raman spectra were collected on an LabRAM Odyssey Raman spectrometer system (HORIBA) using a 532 nm wavelength laser combined with the LAND battery testing equipment. The Raman shift was adjusted according to the prior calibration done with a Si wafer. The optical measurements were conducted with the microscope integrated with the Raman system. Powder X-ray diffraction (XRD) measurements were conducted on a Bruker D8 Advance with Cu K_α radiation (λ=1.5418), from 5° to 80°. The inductive coupled plasma emission spectrometer measurements were conducted with the Aglient ICPOES730 equipment.

Evaluaiton of Oxygen Electrocatalytic Activitiy

For the oxygen reduction reaction (ORR) measurements, a fresh air electrode galvanostatically held at 1.3 V vs. Zn for 60 min was directly severed as the working electrode, and a graphite rod and an Ag/AgCl electrode (3 M KCl, aq) were used as the counter electrode and reference electrode, respectively. All the potentials were referred to RHE. The electrolyte used was 2 M NH_4Cl and 0.5 M $ZnCl_2$ aqueous solution. The linear sweep voltammetry measurements were conducted in the range of 0.3 V – 1.0 V *vs.* RHE with a cathodic scan under O_2 or Ar atmosphere. For evaluation of oxygen evolution reaction (OER), similar components were used to the ORR measurement except for the use of a fully charged air electrode (galvanostatic charged at 0.5 mA cm^{-2} for 2 h) in the DCS-ZAB as the working electrode, and 2M NH_4Cl aqueous solution as electrolyte. The cyclic voltammetry measurements were conducted in the potential range of 1.2 V – 1.8 V *vs.* RHE. The 20 wt% Pt/C and IrO_2 mixture (mass ratio 1:1) loaded on the carbon paper (mass loading of 1 mg cm^{-2}) were also investigated with the same procedure for comparison.

Synthesis of Cu_2O electrode

Cu_2O was electrochemically deposited on an acidified hydrophilic carbon paper at -0.5 V vs Ag/AgCl for 15 minutes in a three-electrode setup, using an electrolyte of 0.1 M $Cu(CH_3COO)_2$ (monohydrate, ≥ 99 %, Merck) and 0.1 M $NaCH_3COO$ (anhydrous, ≥ 99.0%, Sigma Aldrich). The carbon paper was the working electrode while a graphite rod was used as the counter electrode and an Ag/AgCl electrode as the reference electrode. After the electrodeposition, the carbon paper was rinsed with deionized water and dried in the air overnight. The structural composition of the synthesized Cu_2O was confirmed with XRD.

Theoretical calculations

All the calculations were performed by the Vienna ab initio simulation package (VASP)[1] using periodic density functional theory (DFT). Generalized gradient approximation (GGA) of Perdew−Burke−Ernzerhof was supplemented. Projector augmented wave (PAW) method[2] was employed to describe valence-electron interactions. Spin polarization was employed when necessary. The Brillouin zone was sampled with a (2×2×1) Gamma-point-centered k-point grid. Energy cutoff

was set to 350 eV and electron smearing was employed using Gaussian smearing technique with a width of 0.2 eV. For geometries relaxations, electronic energies were computed with the SCF tolerance of 10^{-6} eV and total forces were converged to less than 0.03 eV/Å. For density of states calculations, the "+U" description [3] was employed with the energy converged to 10^{-6} eV. The Hubbard U value of Mn and Cu atoms was chosen as 4.5 eV and 6.0 eV. The free energy profile was calculated referring to the standard hydrogen electrode model reported by Nørskov et al.[4, 5] The overall oxygen electrochemical reactions are divided into four elementary steps:

(1) $O_2(g) + H_2O\,(l) + e^- + * = OOH^* + OH^-$

(2) $OOH^* + e^- = O^* + OH^-$

(3) $O^* + H_2O\,(l) + e^- = OH^* + OH^-$

(4) $OH^* + e^- = * + OH^-$

where the asterisk denotes a surface-bound species. The overall steps of OER are the reverse reactions of ORR. The free energy changes were then calculated as the difference between the products and reactants in each step, as shown below:

$$\Delta G = \Delta E + \Delta ZPE - T\Delta S \qquad (2)$$

where Δ E is the calculated total energy of the reaction, ZPE is the zero-point energy, S is the entropy.

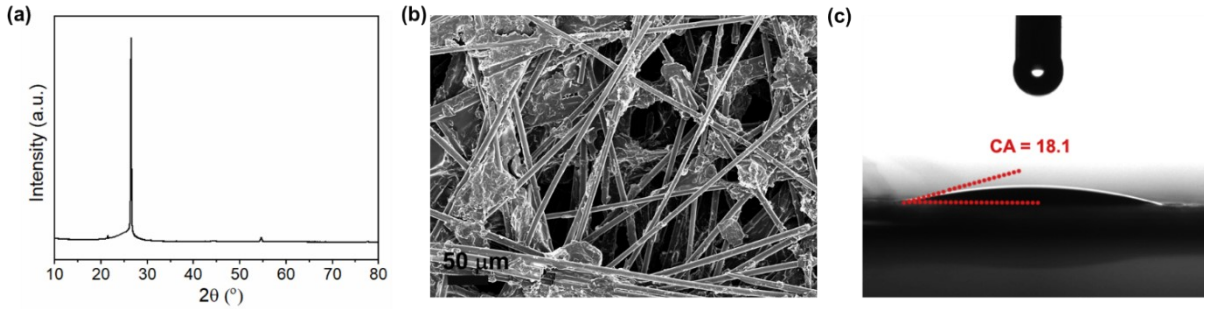

Fig. S1. The characterizations of the acidified carbon paper. (a) XRD patterns, (b) SEM image and (c) the contact angle measurement.

As shown in Fig. S1**,** the XRD patterns (Fig. S1a) of the acidified carbon paper shows a large

peak around 28°, corresponding to (002) peak of the graphitized carbon. The SEM image (Fig. S1b) shows the interconnected fibers with diameters of ~80 μm. The contact angle measurement (Fig. S1c) shows the acidified carbon paper is hydrophilic (CA =18.1°).

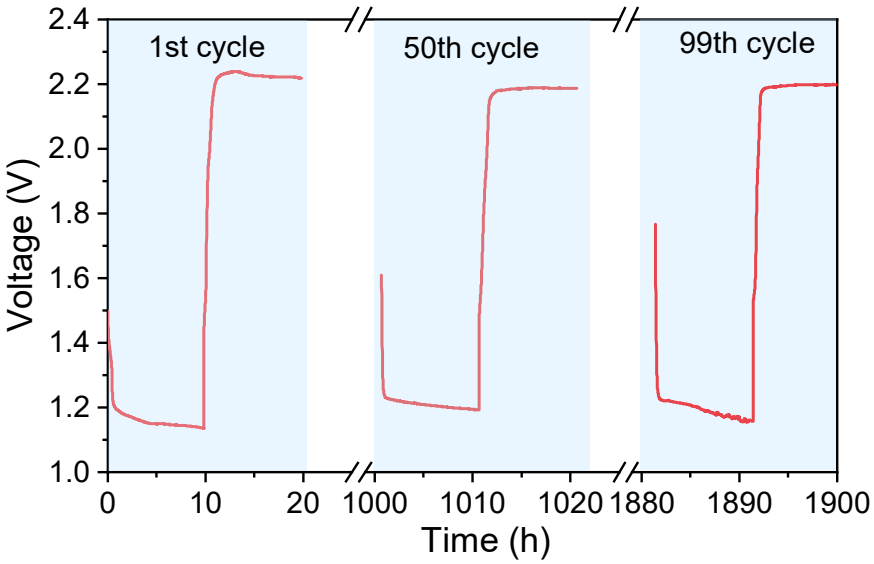

Fig. S2. The charge and discharge plots of the DSC-ZAB under different cycles.

Table S1. The concentration of electrolyte before and after cycling.

Fresh electrolyte	Cu(II)	Mn(II)	**Cycled electrolyte**	Cu(II)	Mn(II)
Mass concentration	738.7 mg/L	234.7 mg/L	Mass concentration	967.3 mg/L	323.6 mg/L
Molar concentration	0.1162 mol/L	0.04271 mol/L	Molar concentration	0.1517 mol/L	0.05890 mol/L

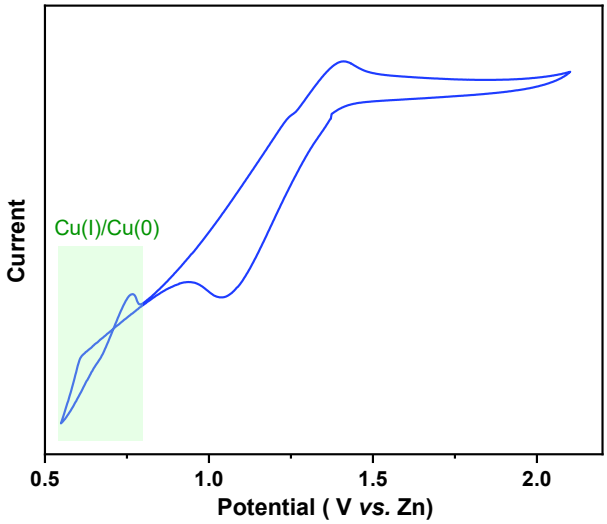

Fig. S3. The CV plot of the ZAB using Cu(II)-only electrolyte. The voltage range is 0.5 V - 2.2 V. An additional redox peaks in the range of 0.5-0.7 V, corresponding to the Cu(I)/Cu(0) reactions.

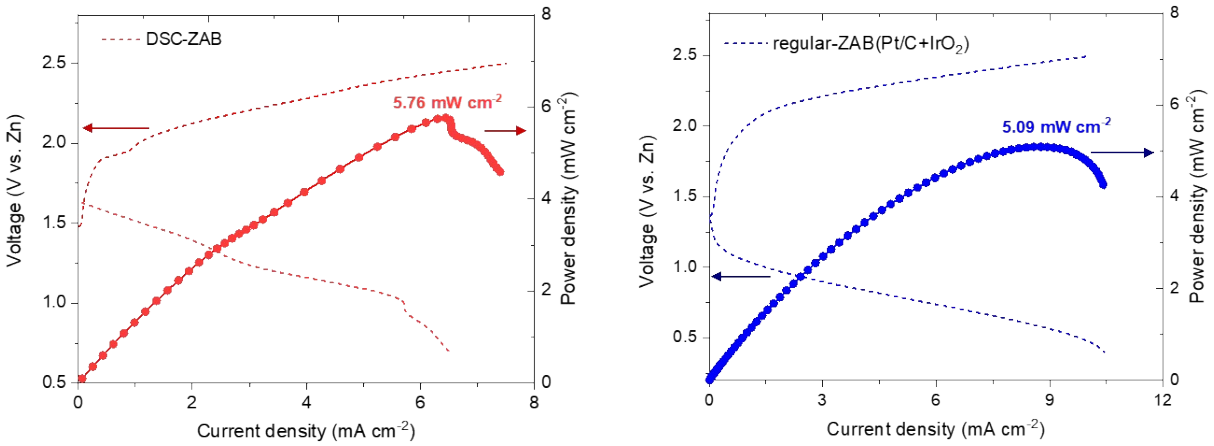

Fig. S4. The discharge and charge plots and corresponding power density curves of different near-neutral ZABs. (a) the DSC-ZAB, (b) the regular ZAB (Pt/C+IrO_2) and (c) the regular-bare-ZAB.

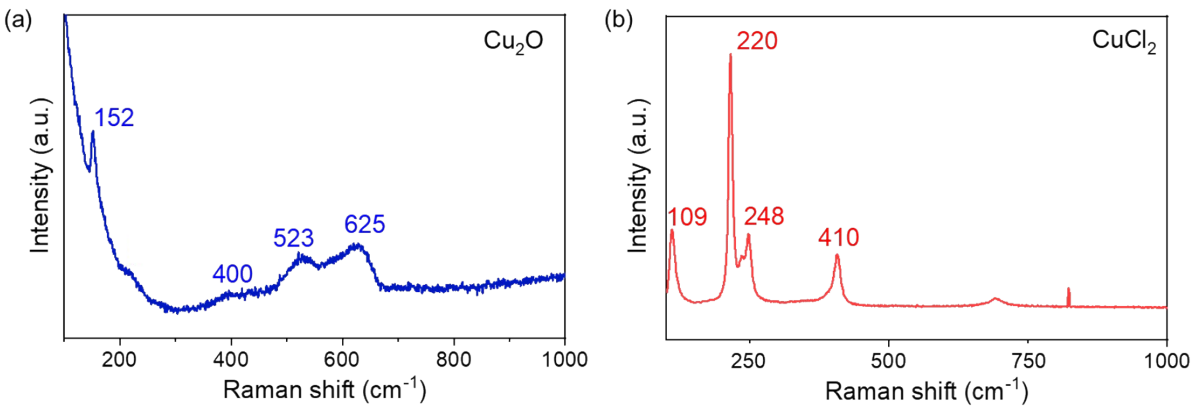

Fig. S5. The Raman spectrum of (a) Cu_2O and (b) $CuCl_2$.

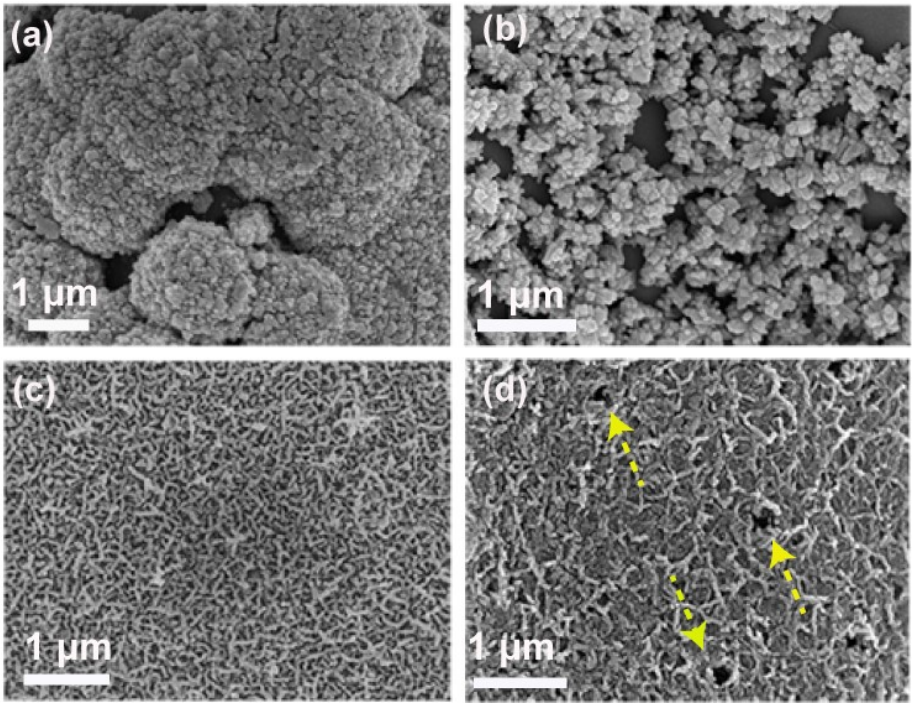

Fig. S6. The ex-situ scanning electron microscopy (SEM) images of air electrodes at different discharge and charge states. (a) Discharged to 1.30 V in the first cycle, (b) charged to 1.70 V in the first cycle, (c) charged to 1.90 V in the first cycle and (d) discharged to 1.5 V in the second cycle.

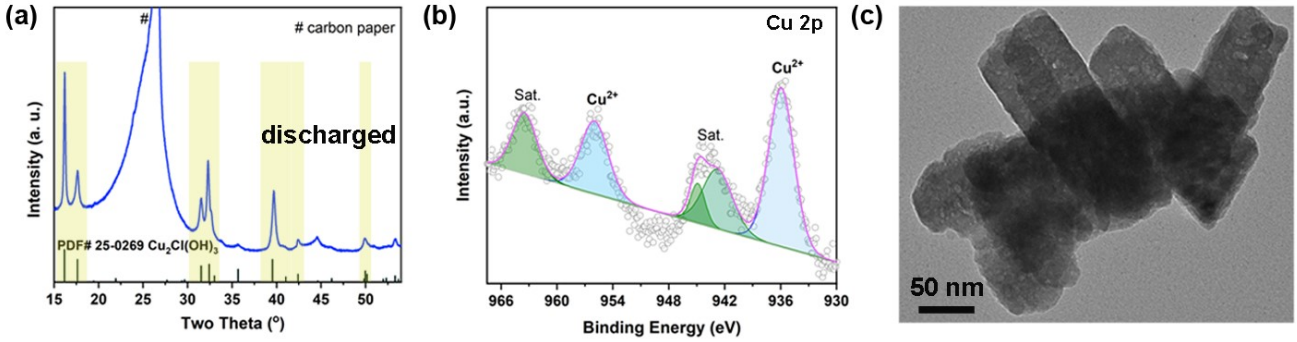

Fig. S7. The characterizations of the discharged air electrode after exposure in air. (a) X-ray diffraction (XRD) pattern, (b) X-ray photoelectron spectroscopy (XPS) spectrum and (c) transmission electron microscopy (TEM) image.

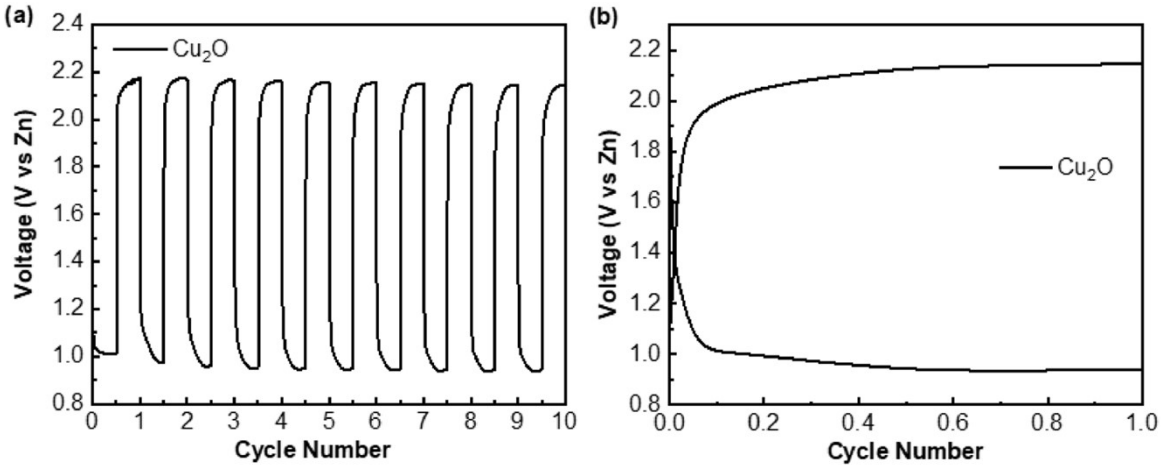

Fig. S8. (a) Cycling performance and (b) Galvanostatic charge-discharge profile of the near-neutral Zn-air batteries (NN-ZAB) using the Cu_2O preloaded electrocatalyst and 2 M NH_4Cl+ 0.5 M $ZnCl_2$ electrolyte with only Mn(II) additive.

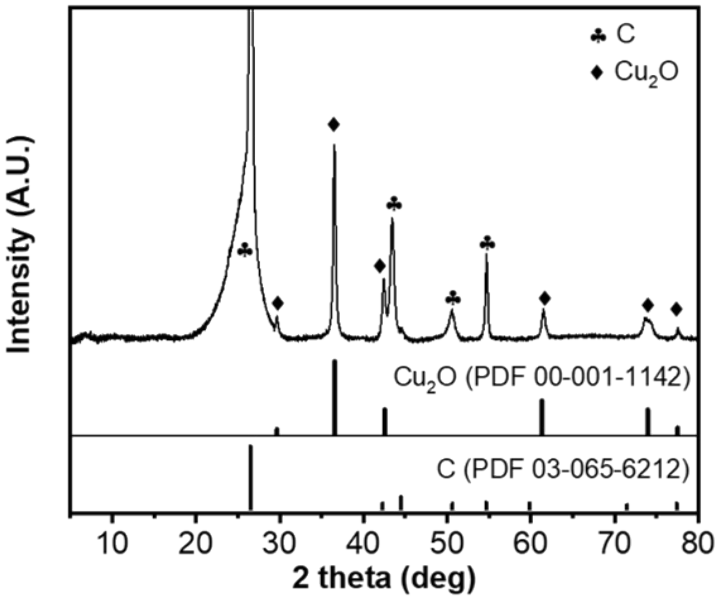

Fig. S9. XRD pattern of the electrodeposited Cu_2O.

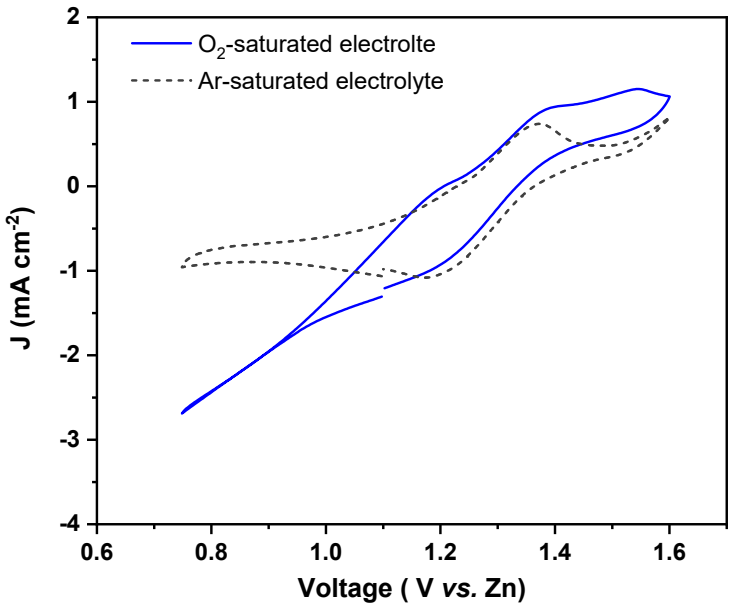

Fig. S10. The CV plot of the DSC after holding at 1.10 V for 2h to deposit the Cu(I)-O-Cl.

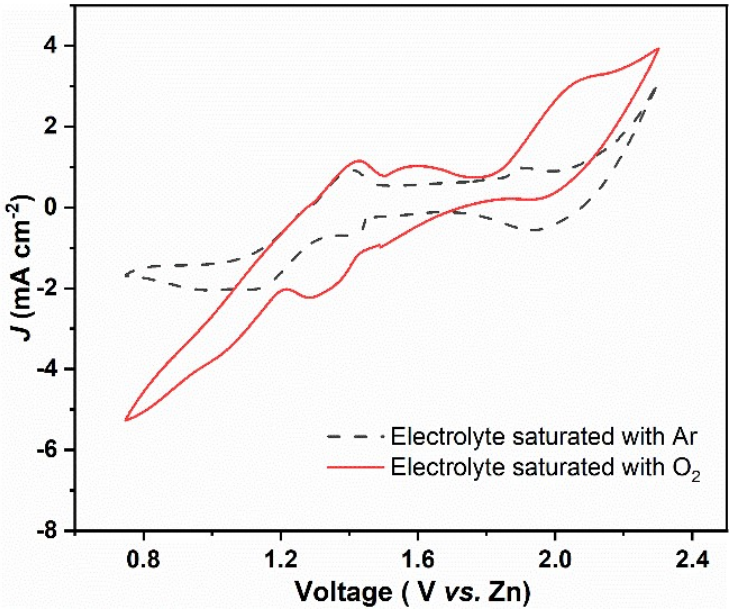

Fig. S11. The cyclic voltammograms of DSC-ZAB with Ar-saturated and O_2-saturated electrolyte.

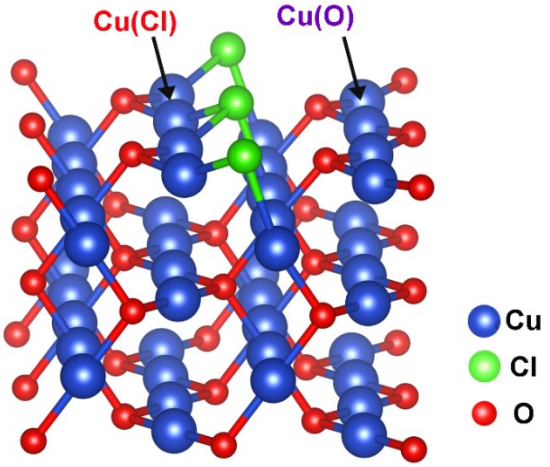

Fig. S12. The structure of Cl-doped Cu_2O (110) surface.

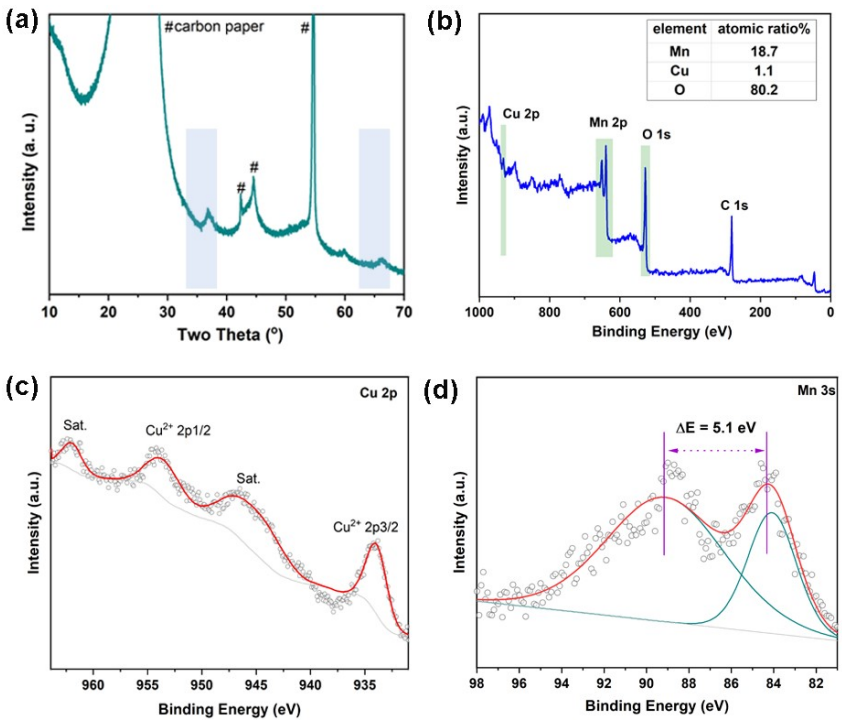

Fig. S13. The characterizations of the charged air-electrode. (a) XRD pattern, (b) XPS spectrum, (c) Cu 2p XPS spectrum and (d) Mn 3s XPS spectrum.

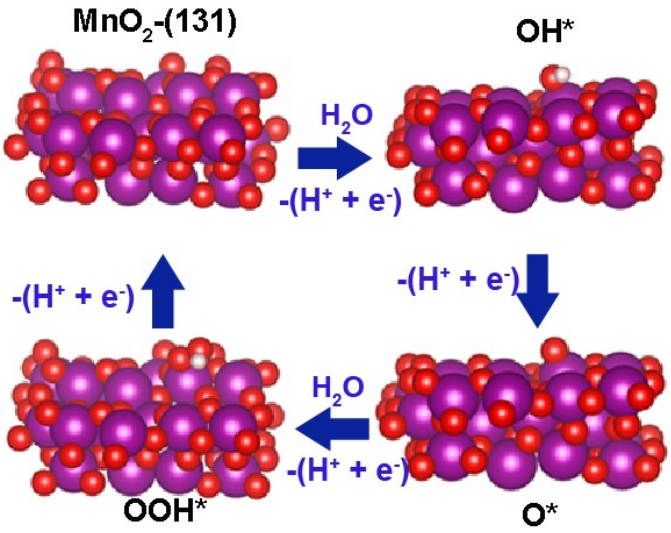

Fig. S14. The optimized structure of MnO_2 (131) surface and the adsorption structures of oxygen intermediators on the MnO_2.

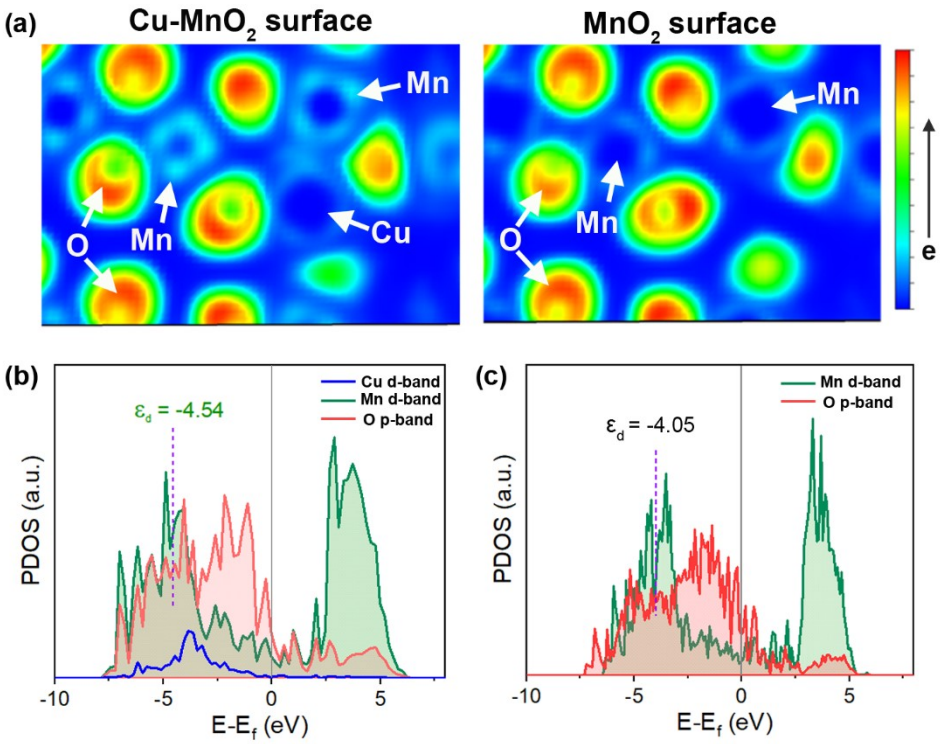

Fig. S15. (a) The Electron Localization Function (ELF) of Cu-MnO_2 (131) surface, comparing with MnO_2 (131) surface. More electron density is revealed around the Mn atom in Cu-MnO_2 (131) surface. (b) The partial DOS for Cu-MnO_2 (131) surface and (c) MnO_2 (131) surface.

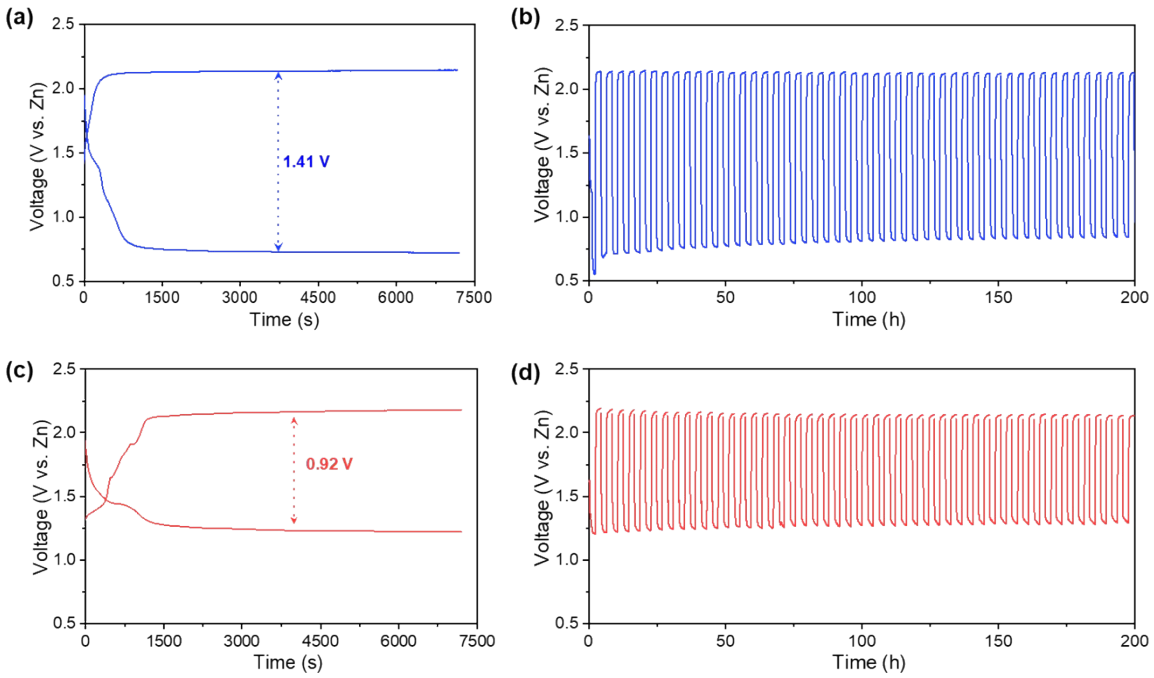

Fig. S16. The battery performances of NN-ZAB using Cu-MnO_2 as preloaded catalyst (NN-ZAB(Cu-MnO_2)) with different catholyte electrolyte. (a) The galvanostatic discharge-charge profiles and (b) cyclic performances of the NN-ZAB(Cu-MnO_2) using 2 M NH_4Cl and 0.5 M $ZnCl_2$ electrolyte. (c) The galvanostatic discharge-charge profiles and (d) cyclic performances of the NN-ZAB(Cu-MnO_2) using 2 M NH_4Cl, 0.5 M $ZnCl_2$ and 0.1M $CuCl_2$ electrolyte. The current density was 0.5 mA cm^{-2}.

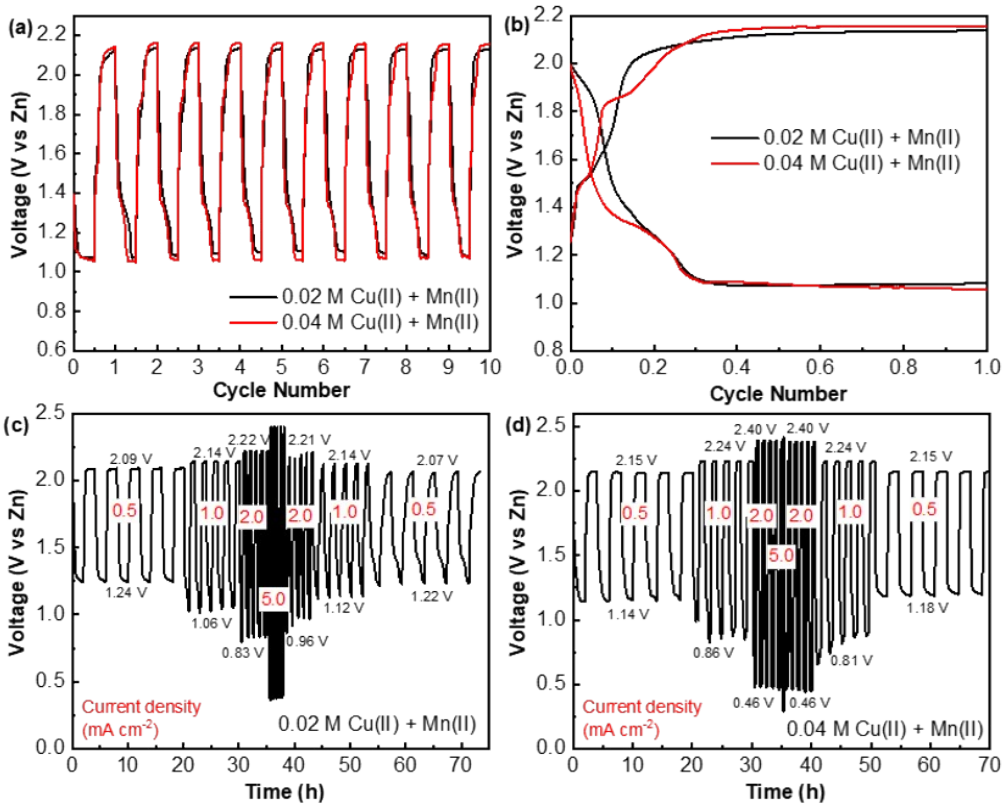

Fig. S17. Battery performance of the NN-ZABs containing different concentration of Cu(II) salt with a fixed amount (0.04 M) of Mn(II) salt. (a) Comparison of the cycling performance via galvanostatic charge and discharge. (b) Corresponding voltage profile of the ZABs in (a). (c, d) Rate performance of the ZABs.

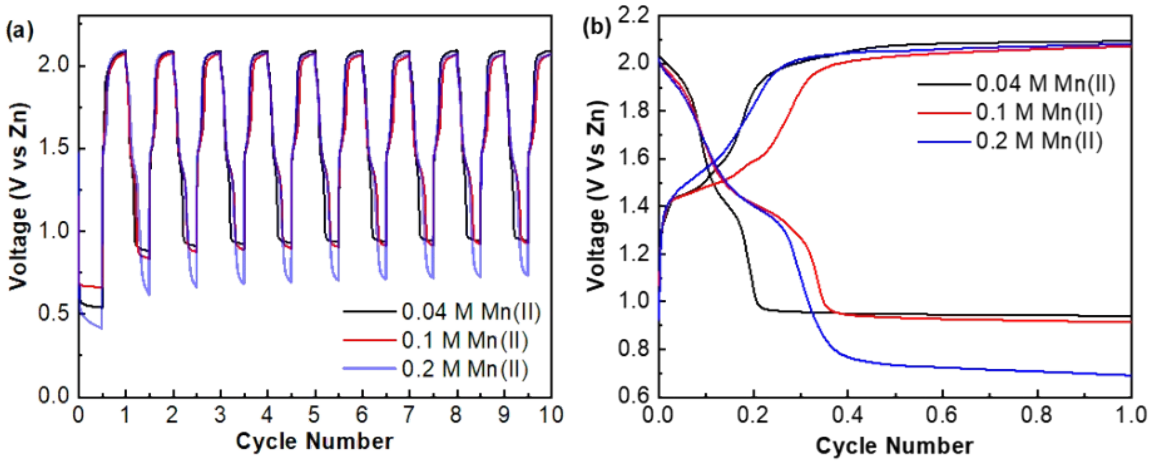

Fig. S18. Battery performance of the NN-ZABs containing only Mn(II) salt at different concentration. (a) Comparison of the cycling performance via galvanostatic charge and discharge. (b) Corresponding voltage profile of the ZABs in (a).

The Fig. S18 shows the batteries performance of NN-ZABs with different concentration of Mn(II) additives in the NH_4Cl-$ZnCl_2$ electrolyte. Although 0.1 M Mn(II) seems to have a slightly lower overpotential for oxygen evolution reaction (OER), 0.04 M Mn(II) is still chosen as the best. This is because, it shows the best reversibility of the deposition-dissolution reaction as determined by the voltage profile (Fig. S18). Poorer reversibility is not favored as it will lead to increasing coverage of MnO_2 which has a poorer electrical conductivity than the carbon substrate. Over time, the available area for the deposition-dissolution reactions (both Mn(II) and Cu(II)) will decrease, which results in a lower utilization of the electrolyte. This can affect the efficiency in the longer term instead.

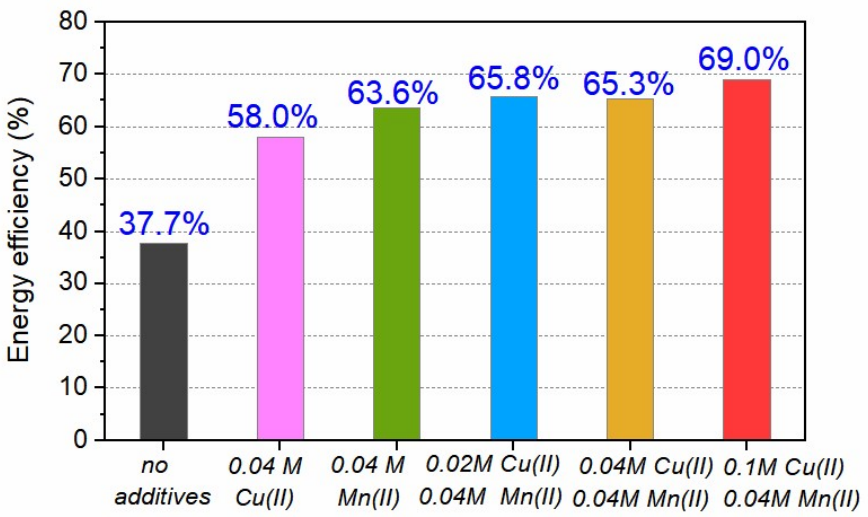

Fig. S19. The energy efficiencies of the NN-ZABs with different concentrations of Cu(II) and Mn(II) additives in the near-neutral electrolyte.

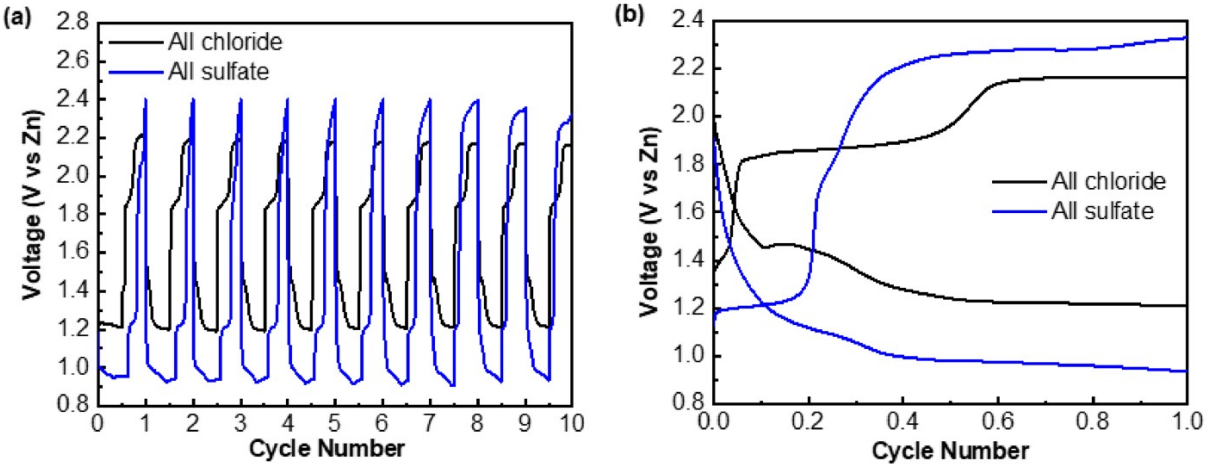

Fig. S20. Electrochemical characterizations of NN-ZABs with either an all-chloride or an all-sulfate electrolyte. (a) Cycling profiles and (b) Discharge-charge profiles of the NN-ZABs.

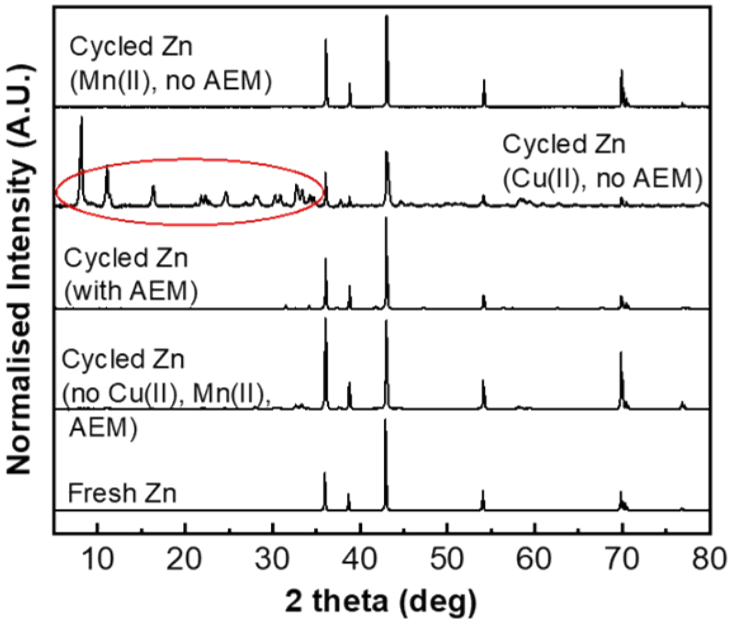

Fig. S21. Comparison of the XRD patterns of the Zn anode in the ZABs after battery cycling. Different configurations (with or without anion-exchange membrane, AEM) and electrolyte compositions (with or without Cu(II) and Mn(II) salts) were adopted.

Table S2. Comparison of reported rechargeable near-neutral Zinc-air batteries (ZABs).

Catalyst	Type	Mass loading (mg cm^{-2})	Electrolyte	Energy efficiency	Cycle life	Ref.
Cu(I)-O-Cl + e-MnO_2	**In-situ generation**	**-/0.25**	**2 M NH_4Cl + 0.5 M $ZnCl_2$ + 0.1 M $CuCl_2$ + 0.04 M $MnSO_4$**	**69.0% @ 0.5 mA cm^{-2}**	**1800 h @ 1 mA cm^{-2}**	**This work**
Co corrole @ Fe_3O_4	Preloaded	1	4.0 M NH_4Cl, 2.0 M KCl, $NH_3 \cdot H_2O$	~43.3% @ 2 mA cm^{-2}	100 h @ 2 mA cm^{-2}	6
FeCo SAs@Co/N-GC	Preloaded	1	3 M $Zn(TFSI)_2$	~68.2% @ 5 mA cm^{-2}	300 h @ 5 mA cm^{-2}	7
SA-Ir/NC	Preloaded	0.5	0.1 M PBS solution, 0.02 M $Zn(CH_3COO)_2$	Not reported	100 h @ 5 mA cm^{-2}	8
$MnS_{0.10}O_{1.90}$/ $MnCo_2S_4$	Preloaded	2	5 M NH_4Cl, 0.25 M $ZnCl_2$ solution	Not reported	140 h @ 10 mA cm^{-2}	9
h-$MnO_xP_{0.21}$ /h-Co-$MnO_xP_{0.21}$	Preloaded	2	2 M NH_4Cl, 0.1 M $ZnCl_2$, $NH_3 \cdot H_2O$	~40.9% @ 1 mA cm^{-2}	700 h @ 1 mA cm^{-2}	10
Fe/Fe_3C@N-doped carbon nanotubes	Preloaded	1.5	4 M NH_4Cl + 2 M KCl	Not reported	208 h @ 2 mA cm^{-2}	11
Co_3O_4 nanosheets	Preloaded	-	PVA + NH_4Cl + $ZnCl_2$	~36% @ 1 mA cm^{-2}	70 h @ 1 mA cm^{-2}	12
MnO_2 + CNT	Preloaded	11	2.34 M NH_4Cl + 0.51 M $ZnCl_2$	46.44% @ 0.5 mA cm^{-2}	400 h @ 0.5 mA cm^{-2}	13
$NiFe_2O_4$/$FeNi_2S_4$ nanosheets	Preloaded	-	4 M NH_4Cl + 2 M KCl	46.7% @ 0.5 mA cm^{-2}	150 h @ 0.5 mA cm^{-2}	7
MnO_x	Preloaded	-	5 M NH_4Cl + 35 g L^{-1} $ZnCl_2$ + 1000 ppm thiourea	51.5% @ 1 mA cm^{-2}	2160 h @ 1 mA cm^{-2}	14

References:

1. G. Kresse and J. Furthmüller, *Phys. Rev. B*, 1996, **54**, 11169-11186.
2. P. E. Blöchl, *Phys. Rev. B*, 1994, **50**, 17953-17979.
3. S. L. Dudarev, G. A. Botton, S. Y. Savrasov, C. J. Humphreys and A. P. Sutton, *Phys. Rev. B*, 1998, **57**, 1505-1509.
4. J. K. Nørskov, J. Rossmeisl, A. Logadottir, L. Lindqvist, J. R. Kitchin, T. Bligaard and H. Jónsson, *J Phys. Chem. B, 2004, **108**, 17886-17892.*
5. J. Rossmeisl, Z. W. Qu, H. Zhu, G. J. Kroes and J. K. Nørskov, *J. Electroanal. Chem.*, 2007, **607**, 83-89.
6. L. Xie, X. Li, B. Wang, J. Meng, H. Lei, W. Zhang and R. Cao, *Angew. Chem. Int. Ed.*, 2019, **58**, 18883-18887.
7. L. An, Z. Zhang, J. Feng, F. Lv, Y. Li, R. Wang, M. Lu, R. B. Gupta, P. Xi and S. Zhang, *J. Am. Chem. Soc.*, 2018, **140**, 17624-17631.
8. X. Luo, M. Yang, W. Song, Q. Fang, X. Wei, L. Jiao, W. Xu, Y. Kang, H. Wang, N. Wu, W. Gu, L. Zheng, L. Hu and C. Zhu, *Adv. Funct. Mater.*, 2021, **31**, 2101193
9. K. Wang, Z. Wang, Y. Liu, J. Liu, Z. Cui, X. Zhang, F. Ciucci and Z. Tang, *Chem. Eng. J.*, 2022, **427**, 131966
10. T. Zhang, S. Zhang, S. Cao, Q. Yao and J. Y. Lee, *Chem. Mater.* , 2018, **30**, 8270-8279.
11. X. Wei, S. Song, N. Wu, X. Luo, L. Zheng, L. Jiao, H. Wang, Q. Fang, L. Hu, W. Gu, W. Song and C. Zhu, *Nano Energy*, 2021, **84**.
12. Y. Li, X. Fan, X. Liu, S. Qu, J. Liu, J. Ding, X. Han, Y. Deng, W. Hu and C. Zhong, *J. Mater. Chem. A*, 2019, **7**, 25449-25457.
13. E. Iruin, A. R. Mainar, M. Enterria, N. Ortiz-Vitoriano, J. A. Blazquez, L. C. Colmenares, T. Rojo, S. Clark and B. Horstmann, *Electrochim. Acta*, 2019, **320**, 134557.
14. A. Sumboja, X. Ge, G. Zheng, F. W. T. Goh, T. S. A. Hor, Y. Zong and Z. Liu, *J. Power Sources* 2016, **332**, 330-336.